Renewable Energy

Sensorless Adaptive Control of Brushless Doubly-Fed Reluctance Generators for Wind Power Applications

--Manuscript Draft--

Manuscript Number:	RENE-D-21-00494R1
Article Type:	Research Paper
Keywords:	Doubly Fed Generators; Wind Energy Conversion Systems; Sensorless Control; Power Control
Corresponding Author:	M. R. Agha Kashkooli, Ph.D Northumbria University Faculty of Engineering and Environment Newcastle upon Tyne, Tyne and Wear UNITED KINGDOM
First Author:	M. R. Agha Kashkooli, Ph.D
Order of Authors:	M. R. Agha Kashkooli, Ph.D
	Milutin Jovanovic, Ph.D.
Abstract:	A novel model reference adaptive system for the rotor position/speed estimation and sensorless operation of a brushless doubly fed reluctance generator with maximum power point tracking is presented. Its main advantage over the existing designs are the inherent robustness and stability afforded by the complete parameter independence of the reference model using only the measured currents of the converter-fed (secondary) winding. In addition, the respective stationary frame current components are estimated by the adaptive model using the voltage and current measurements of the grid-connected (primary) winding at line frequency, offering higher accuracy. The simulation and experimental results have demonstrated the excellent real and reactive power controller performance for typical operating characteristics of wind turbines.

Sensorless Adaptive Control of Brushless Doubly-Fed Reluctance Generators for Wind Power Applications

M. R. Agha Kashkooli[a,*], Milutin G. Jovanović[a]

[a]*Faculty of Engineering and Environment, Northumbria University, Newcastle upon Tyne, United Kingdom*

ABSTRACT

A novel model reference adaptive system for the rotor position/speed estimation and sensorless operation of a brushless doubly fed reluctance generator with maximum power point tracking is presented. Its main advantage over the existing designs are the inherent robustness and stability afforded by the complete parameter independence of the reference model using only the measured currents of the converter-fed (secondary) winding. In addition, the respective stationary frame current components are estimated by the adaptive model using the voltage and current measurements of the grid-connected (primary) winding at line frequency, offering higher accuracy. The simulation and experimental results have demonstrated the excellent real and reactive power controller performance for typical operating characteristics of wind turbines.

Keywords: Doubly Fed Generators; Wind Energy Conversion Systems; Sensorless Control; Power Control.

1. Introduction

A doubly fed induction generator (DFIG) has been traditionally used as an economical solution for wind energy conversion systems (WECS) with limited speed ranges (e.g. 2:1 or so) [1, 2]. However, the cost benefits of a fractional converter (normally around 30% of the DFIG rating) and its relatively low failure rates reported in practice [3] are offset by the compromised reliability and maintenance issues of brushes and slip-rings.

The emerging, medium-speed Brushless Doubly Fed Reluctance Generator (BDFRG), shown in Fig. 1, is a DFIG alternative for WECS [4–6]. As a member of the doubly-fed machines family, it can use a similar partially-rated converter, but with virtually no maintenance requirements making it more cost-effective and reliable than the DFIG. Unlike the latter, the BDFRG has a conventional sinusoidal double wound stator with different pole numbers and applied frequencies, and a modern multi-barrier cage-less reluctance rotor having half the total number of the stator poles [7]. The functionality and roles of the BDFRG windings are otherwise identical to DFIG's: the primary (power) winding is grid-tied directly, and the secondary (control) one through a back-to-back converter to allow bi-directional power flow for super-synchronous or sub-synchronous speed variations by analogy to the DFIG rotor winding. Such unusual design and operating principles bring another important reliability and cost advantage over DFIG: a 50% reduction of the 'natural' synchronous speed for the same number of rotor poles and line frequency. This implies that a compact, simpler and more efficient two-stage gearbox can be used for BDFRG wind turbines instead of a problematic three-stage counterpart of DFIG, susceptible to failures [8–10]. The BDFRG also offers the prospects for superior low voltage fault ride through properties to DFIG due to the comparatively higher leakage inductances and lower inrush currents, and competitive frequency support provision [11].

By virtues of the fixed switching rates and low total harmonic distortion contrary to the hysteresis type [12], vector control has been a dominant choice for WECS either using the industrial DFIG [13] or BDFRG prototypes [14–16]. However, if shaft encoders were needed for this purpose, the sturdiness and reliability of a drive train would be diminished and maintenance requirements increased. The research and development of sensorless control strategies for both DFIG [17–23] and BDFRG [24–27] have been gaining a lot in popularity recently to overcome this limitation.

A viable rotor angular position and velocity state observer has been applied for flux (field) oriented control of the BDFRG in [24, 25]. However, the sensitivity to machine parameter knowledge has not been addressed and substantiated in this work. The model reference adaptive system (MRAS) based substitutes using the same control method

*Corresponding author

mohammad.kashkooli@northumbria.ac.uk (M. R. Agha Kashkooli)

ORCID(s): 0000-0001-7511-2910 (M. R. Agha Kashkooli)

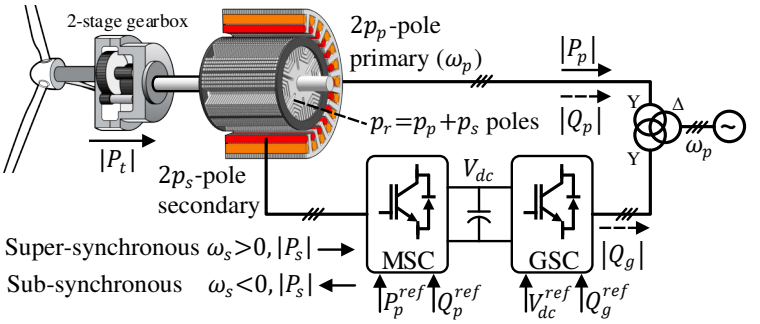

Figure 1: An outline of a wind energy conversion system using the BDFRG.

as in [25] have been proposed in [26] and [27]. The erroneous secondary-flux estimates at typically low fundamental frequencies have hindered the controller stability over the whole speed range [26]. Performance improvements have been achieved using the secondary real power as the reference model foundation [27]. However, although the adaptive model in [27] is dependent on both the secondary winding resistance (R_s) and mutual inductance (L_m), the sensitivity analyses to R_s uncertainties have only been presented, but not to L_m variations being much more important for the observer convergence and accuracy. The MRAS observer design in [28] brings additional advantages by introducing the measurable secondary currents as the reference model outputs, while the corresponding estimates are entirely based on the primary quantities at fixed line-frequency. The requirement for the flux identification and resistance knowledge of the primary winding is the main drawback of the adaptive model in [28]. Furthermore, the associated results are produced for a small BDFRG prototype with relatively limited industrial interest for wind power applications.

A new, closed-loop MRAS estimator for the rotor angular velocity and position identification and encoder-less control of the large-scale BDFRG has been put forward in this paper. The proposed design is more robust and easier to implement than the Luenberger-style observer considered in [24, 25]. The measurable stationary frame secondary currents have served as the outputs of the parameter-free reference model, with the primary winding measurements of fixed line voltage and frequency being used by the adaptive model to generate the corresponding estimates. Such an observer configuration can ensure the higher estimation quality and fewer parameter dependence than the MRAS equivalents in [26, 27]. Comprehensive sensitivity studies to inductance mismatches have been conducted to underpin the realistic simulations and hardware-in-the-loop test results for a 1.5 MW BDFRG wind turbine.

2. BDFRG Fundamentals

The rotor angular velocity and position of the BDFRG, conceptually shown in Fig. 1, can be expressed as [14, 15]:

$$\omega_{rm} = \frac{\omega_p + \omega_s}{p_r} = \frac{\omega_p}{p_r}\left(1 + \frac{\omega_s}{\omega_p}\right) = \omega_{syn}\left(1 + \frac{\omega_s}{\omega_p}\right) \tag{1}$$

$$\theta_{rm} = \frac{\theta_r}{p_r} = \frac{\theta_p + \theta_s}{p_p + p_s} \tag{2}$$

If the secondary winding is DC (i.e $\omega_s = 0$), the BDFRG is in synchronous mode running at $\omega_{syn} = \omega_p/p_r$, which is half that of a p_r-pole DFIG given (1). Thus, the BDFRG is a medium-speed machine requiring a two-stage gearbox and avoiding the troublesome high speed (3rd) stage of DFIG [29].

Using (1), the BDFRG mechanical power relationship in steady-state can be formulated as follows:

$$P_m = T_e \cdot \omega_{rm} = \underbrace{\frac{T_e \cdot \omega_p}{p_r}}_{P_p} + \underbrace{\frac{T_e \cdot \omega_s}{p_r}}_{P_s} = P_s \cdot \left(1 + \frac{\omega_p}{\omega_s}\right) \tag{3}$$

$$= P_p \cdot \left(1 + \frac{\omega_s}{\omega_p}\right) = P_p \cdot \left(1 + \frac{f_s}{f_p}\right) \tag{4}$$

where the electro-magnetic torque, $T_e < 0$, and the primary power, $P_p < 0$ (i.e. $P_p > 0$ delivered to the grid), with the adopted *motoring* (BDFRM) convention. Note from (3) and Fig. 1 that the secondary power flow (P_s) can be bi-directional: at super-synchronous speeds $\omega_s > 0$ and $P_s < 0$ (i.e. $P_s > 0$ to the grid), and in sub-synchronous region $\omega_s < 0$ (meaning the opposite phase sequence of the secondary to the primary winding) for $P_s > 0$. The latter speed mode is inefficient as a portion of P_p is circulated through the machine via the converter producing losses.

The slip power recovery of the BDFRG is hidden in the following ratio for a given speed range around ω_{syn}:

$$a = \frac{\omega_{max}}{\omega_{min}} = \frac{\omega_{syn} + \Delta\omega}{\omega_{syn} - \Delta\omega} = \frac{\omega_p + \omega_s}{\omega_p - \omega_s} \Longrightarrow \frac{\omega_s}{\omega_p} = \frac{a-1}{a+1} \tag{5}$$

Hence, for a typical $a = 2$, the maximum secondary frequency becomes $\omega_s = \omega_p/3$ and $P_s \approx 0.25 P_m$ according to (3). This means that only a 25% rated converter would ideally do for the power exchange with the grid as with the DFIG. Further details about the BDFRG operating principles and space-vector theory can be found in [30, 31].

3. Dynamic Modelling and Control

The BDFRM(G) $d-q$ equations in rotating reference frames using standard notation in complex form are [14, 15]:

$$\underline{v}_p = R_p \underline{i}_p + \frac{d\underline{\lambda}_p}{dt} + j\omega_p \underline{\lambda}_p \tag{6}$$

$$\underline{v}_s = R_s \underline{i}_s + \frac{d\underline{\lambda}_s}{dt} + j\omega_s \underline{\lambda}_s \tag{7}$$

$$\underline{\lambda}_p = L_p \underline{i}_p + L_m \underline{i}^*_{sm} = L_p(i_{pd} + j i_{pq}) + L_m(i_{md} - j i_{mq}) \tag{8}$$

$$\underline{\lambda}_s = L_s \underline{i}_s + L_m \underline{i}^*_{pm} = \sigma L_s \underline{i}_s + \frac{L_m}{L_p} \underline{\lambda}^*_p = \sigma L_s \underline{i}_s + \underline{\lambda}_m \tag{9}$$

$$T_e = \frac{3}{2} p_r \left(\lambda_{pd} i_{pq} - \lambda_{pq} i_{pd}\right) = \frac{3}{2} p_r \left(\lambda_{md} i_{sq} - \lambda_{mq} i_{sd}\right) \tag{10}$$

where $L_{m,p,s}$ are the magnetising, primary and secondary inductances, $\sigma = 1 - L_m^2/(L_p L_s)$ is the leakage coefficient, λ_m is the mutual flux linkage, and $\underline{i}_{sm}$ is the frequency modulated secondary current vector ($\underline{i}_s$) rotating at ω_p and ω_s, respectively, as shown in Fig. 2. The following flux oriented control form relationships hold [14, 15, 25]:

$$\underbrace{\underline{i}_{sm} = i_{md} + j i_{mq} = i_{sm} e^{j\gamma}}_{d_p - q_p \, frame} \Leftrightarrow \underbrace{\underline{i}_s = i_{sd} + j i_{sq} = i_s e^{j\gamma}}_{d_s - q_s \, frame} \tag{11}$$

The magnetic coupling between the windings is achieved through the modulating actions of the reluctance rotor with half the total number of the stator poles. As a consequence, the resulting harmonic side-bands, rather than the fundamental component, of the air-gap flux are torque producing. Periodic pulsations of the self and mutual inductances with the rotor position are small compared to their average values used in (8) and (9) [30, 31].

Under the primary voltage alignment conditions (i.e $v_{pq} = v_p$, $v_{pd} = 0$) depicted in Fig. 2, ignoring the winding resistance (R_p) as usual for MW range generators, and substituting (6) and (8) into $P_p + jQ_p = 1.5 \cdot \underline{v}_p \underline{i}^*_p$ for $\lambda_{pd} \approx \lambda_p = v_p/\omega_p$, $\lambda_{pq} \approx 0$, and $i_{md} = i_{sd}$ and $i_{mq} = i_{sq}$ from (11), the primary real (P_p) and reactive power (Q_p) expressions in terms of the controllable $d_s - q_s$ frame secondary currents (i_{sd} and i_{sq}) can be derived as follows:

$$\frac{2}{3} P_p = v_p i_{pq} = \frac{\lambda_{pq} + L_m i_{mq}}{L_p} v_p \approx \frac{L_m}{L_p} v_p i_{sq} \tag{12}$$

$$\frac{2}{3} Q_p = v_p i_{pd} = \frac{\lambda_{pd} - L_m i_{md}}{L_p} v_p \approx \frac{v_p}{L_p} \left(\frac{v_p}{\omega_p} - L_m i_{sd}\right) \tag{13}$$

It is worth mentioning that neglecting R_p implies much simpler and faster calculations of the primary flux magnitude ($\lambda_p \approx v_p/\omega_p$) with marginal error, by-passing so the voltage integration issues (e.g. dc offset) to estimate λ_{pq} and λ_{pd} used in (12) and (13). Since v_p and ω_p are constant in magnitude, P_p and Q_p control via i_{sq} and i_{sd} is intrinsically decoupled according to (12) and (13) and can be realised as in Fig. 3. Any inductance knowledge inaccuracies can be handled by the correctly tuned PI gains as will be demonstrated by the results presented in the sequel.

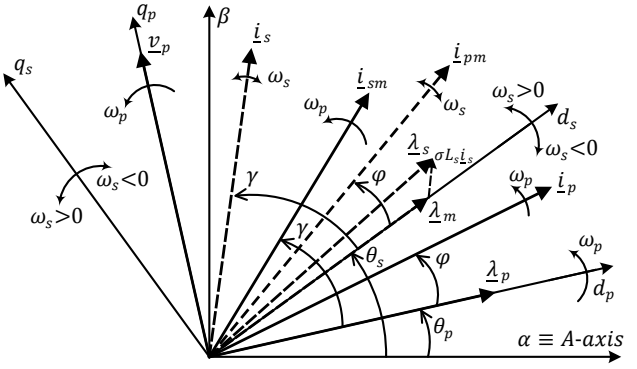

Figure 2: The BDFRG phasor diagram.

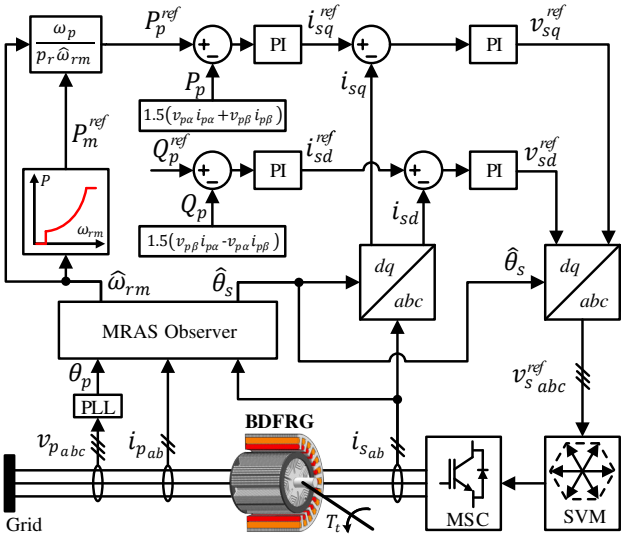

Figure 3: The BDFRG sensorless voltage oriented controller.

4. Rotor Position and Speed Estimation

Generally, the MRAS observer principle is premised on the comparison of adaptive and reference models outputs for the suggested functional quantity. The error between the two models is being driven to zero using a closed-loop adaptation mechanism (e.g. PI controller) to estimate the rotor position by continuously updating the adaptive model in a recursive fashion. As shown in Fig. 3, the estimated speed is used to obtain the maximum power point of the turbine, and the position estimates for the frame transformation within the current control loops. The proposed observer design is given in Fig. 4A. The reference model is highly accurate as being purely based on the secondary current measurements to derive the respective $i_{s\alpha}$ and $i_{s\beta}$ outputs in a stationary $\alpha - \beta$ frame (Figs. 2 and 4B). For a Y-connected winding with a positive phase sequence and no neutral connection, these are as follows:

$$\underline{i}_s = i_s e^{j\delta} = i_{s\alpha} + j i_{s\beta} = i_{sa} + j \frac{i_{sa} + 2 i_{sb}}{\sqrt{3}} \tag{14}$$

Considering (11) and Fig. 2, the magnetically coupled secondary currents in the $d_p - q_p$ frame, $\hat{i}_{mq}$ and $\hat{i}_{md}$, are the same as the source components in the $d_s - q_s$ frame, $\hat{i}_{sq}$ and $\hat{i}_{sd}$. They can be estimated from the measurable i_{pq} and i_{pd} in the $d_p - q_p$ frame applying (8) in the following manner:

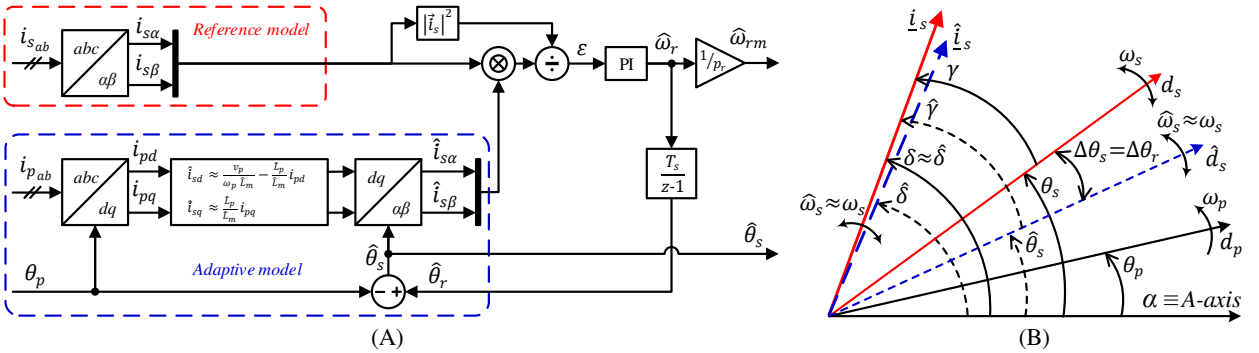

Figure 4: The MRAS observer: A) Block scheme; B) Phasor diagram with characteristic vectors and reference frames.

$$\hat{i}_{mq} = \hat{i}_{sq} = \frac{-\lambda_{pq} + \hat{L}_p i_{pq}}{\hat{L}_m} \approx \frac{\hat{L}_p}{\hat{L}_m} i_{pq} \tag{15}$$

$$\hat{i}_{md} = \hat{i}_{sd} = \frac{\lambda_{pd} - \hat{L}_p i_{pq}}{\hat{L}_m} \approx \frac{v_p}{\omega_p \hat{L}_m} - \frac{\hat{L}_p}{\hat{L}_m} i_{pd} \tag{16}$$

$$i_{pd} + j i_{pq} = (i_{p\alpha} + j i_{p\beta}) e^{-j\theta_p} \tag{17}$$

where $\hat{L}_m$ and $\hat{L}_p$ are the inductance values acquired by off-line testing, whereas $i_{p\alpha}$ and $i_{p\beta}$ are obtained from the measured primary currents using the equivalent of (14).

A usual $d_s - q_s$ to $\alpha - \beta$ frame conversion, $\underline{i}_{\alpha\beta} = \underline{i}_{dq} e^{j\theta_s}$, similar to the $d_p - q_p$ one in (17), can now be used to calculate:

$$\hat{i}_{s\alpha} = \hat{i}_{sd} \cos(\hat{\theta}_r - \theta_p) - \hat{i}_{sq} \sin(\hat{\theta}_r - \theta_p) \tag{18}$$

$$\hat{i}_{s\beta} = \hat{i}_{sd} \sin(\hat{\theta}_r - \theta_p) + \hat{i}_{sq} \cos(\hat{\theta}_r - \theta_p) \tag{19}$$

where $\hat{\theta}_s = \hat{\theta}_r - \theta_p$ (Fig. 4B) and $\hat{\theta}_r = p_r \hat{\theta}_{rm}$ are the estimated control frame and rotor 'electrical' positions using (2).

The normalised error of the adaptive model is defined as:

$$\varepsilon = \frac{\hat{\underline{i}}_s \times \underline{i}_s}{i_s^2} = \frac{\hat{\underline{i}}_s \cdot \underline{i}_s}{i_s^2} \sin\delta_{err} = \frac{\hat{i}_{s\alpha} i_{s\beta} - \hat{i}_{s\beta} i_{s\alpha}}{i_{s\alpha}^2 + i_{s\beta}^2} \tag{20}$$

where $\delta_{err} = \delta - \hat{\delta}$ is the angular misalignment between the actual ($\underline{i}_s$) and estimated ($\hat{\underline{i}}_s$) secondary-current vectors. This is being driven to zero by feeding-back the enhanced $\hat{\theta}_r$ as shown in Fig. 4B. Once $\delta_{err} \approx 0$, then $\tan\hat{\delta} = \hat{i}_{s\beta}/\hat{i}_{s\alpha} \approx \tan\delta = i_{s\beta}/i_{s\alpha}$ i.e. $\hat{i}_s$ and i_s become nearly aligned both rotating at $\hat{\omega}_s \approx \omega_s$. The underlying adaptive scheme to make this happen is devised from a small signal analysis of (20) around the $\delta_{err} \approx 0$, $\cos\delta_{err} \approx 1$, $\hat{i}_s \approx i_s$ steady-state point:

$$\frac{d\varepsilon}{dt} = \frac{\hat{\underline{i}}_s \cdot \underline{i}_s}{i_s^2} \cos\delta_{err} \left(\frac{d\delta}{dt} - \frac{d\hat{\delta}}{dt} \right) \approx \frac{d\delta}{dt} - \frac{d\hat{\delta}}{dt}$$

$$\approx \omega_s - \hat{\omega}_s = (\omega_r - \omega_p) - (\hat{\omega}_r - \omega_p) = \Delta\omega_r \tag{21}$$

$$\varepsilon \approx \int (\omega_r - \hat{\omega}_r) dt = \frac{\omega_r - \hat{\omega}_r}{s} = p_r \frac{\Delta\omega_{rm}}{s} \tag{22}$$

The above relationships clearly indicate that a key factor for the observer stability is the high accuracy of $\hat{\omega}_r$ (i.e $\Delta\omega_r \approx 0 \Rightarrow \dot{\varepsilon} \approx 0$). A PI controller is designed using (22) to obtain the $\hat{\omega}_r$ resulting in $\varepsilon \approx 0$. Adaptive PI tuning under variable loading conditions is provided by the i_s^2 division term in (20).

5. Parameter Mismatch Inferences

The adaptive model, build upon (15)-(19), is contingent on the machine inductances. So, any deviations of $\hat{L}_{m,p}$ from the exact $L_{m,p}$ induced by off-line testing, magnetic saturation or other practical effects, can deteriorate the observer performance. For example, the current estimates generated using (15) and (16) are subject to variances in $\hat{L}_p/\hat{L}_m$ from the actual ratio, whereas $\hat{i}_{sd}$ is additionally influenced by the $\hat{L}_m$ discrepancies. The errors in $\hat{i}_{sq}$ and $\hat{i}_{sd}$ are propagated further by erroneous $\hat{\theta}_r$ through (18) and (19), making $\hat{i}_{s\alpha} \neq i_{s\alpha}$, $\hat{i}_{s\beta} \neq i_{s\beta}$, hence $\hat{i}_s \neq i_s$. The implications of these variations on the position estimation quality, can be better understood by manipulating (18) and (19) using (2) into the form:

$$\tan(\hat{\theta}_r - \theta_p) = \tan\hat{\theta}_s = \frac{\tan\hat{\delta} - \frac{\hat{i}_{sq}}{\hat{i}_{sd}}}{\tan\hat{\delta} + \frac{\hat{i}_{sq}}{\hat{i}_{sd}}} \tag{23}$$

where considering (15) and (16):

$$\frac{\hat{i}_{sq}}{\hat{i}_{sd}} = \frac{\omega_p \hat{L}_p i_{pq}}{v_p - \omega_p \hat{L}_p i_{pd}} = \frac{\omega_p i_{pq}}{v_p/\hat{L}_p - \omega_p i_{pd}} \tag{24}$$

Substituting for (24), (23) can be rearranged as follows:

$$\tan\hat{\theta}_s = \frac{v_p \tan\hat{\delta} - \omega_p \hat{L}_p (i_{pd}\tan\hat{\delta} + i_{pq})}{v_p + \omega_p \hat{L}_p (i_{pq}\tan\hat{\delta} - i_{pd})} \tag{25}$$

It is evident from (23)-(25) that whilst the $\hat{\theta}_r$ and $\hat{\theta}_s$ errors are unaffected by $\hat{L}_m$, they are by the $\hat{L}_p$ inaccuracies, even so, equally, which can be easily confirmed by applying (2):

$$\Delta\theta_r = \theta_r - \hat{\theta}_r = (\theta_s + \theta_p) - (\hat{\theta}_s + \theta_p) = \theta_s - \hat{\theta}_s = \Delta\theta_s \tag{26}$$

The observer ensures that $\varepsilon \approx 0$, hence $\delta_{err} \approx 0$, no matter the inductance mismatch according to (20)-(22). Given that $\hat{\delta} \approx \delta$ is fairly accurate, the $\Delta\theta_r = \Delta\theta_s$ values originating from (23) and (25) purely result from the incorrect $\hat{i}_{sq}/\hat{i}_{sd}$ as both v_p and ω_p are constant, with i_{pd} and i_{pq} being parameter independent, in (24). In fact, for an arbitrary (P_p, Q_p) set-point, the larger the $\hat{L}_p$ in (24), the lower $\hat{i}_{sq}/\hat{i}_{sd}$ (i.e. getting more negative as $i_{pq} \leq 0$), and the greater $\hat{\theta}_r$ and $\hat{\theta}_s$ become looking at (23). In other words, bearing in mind (26), a smaller $\Delta\theta_r = \Delta\theta_s$ would occur if $\hat{L}_p > L_p$ than for $\hat{L}_p < L_p$. This conjecture can be formally verified by differentiating (25) and using the Euler's approximation of the derivative, which after considerable manipulations, and taking into account that $i_{pq} \leq 0$ for the BDFRG, leads to the following expression for the rate of change of $\hat{\theta}_s$ in relation to $\hat{L}_p$:

$$\frac{d\hat{\theta}_s}{d\hat{L}_p} \approx \frac{\Delta\theta_s}{\Delta L_p} = \frac{-\omega_p v_p i_{pq}}{(v_p - \omega_p \hat{L}_p i_{pd})^2 + \omega_p^2 \hat{L}_p^2 i_{pq}^2} \geq 0 \tag{27}$$

where $\Delta L_p = L_p - \hat{L}_p$ and $\Delta\theta_s$ is defined by (26). Therefore, $\hat{\theta}_s$ is increasing with $\hat{L}_p$ so in case of $\hat{L}_p > L_p$ (i.e. $\Delta L_p < 0$) $\Delta\theta_s < 0$, and if $\hat{L}_p < L_p$ (i.e. $\Delta L_p > 0$) then $\Delta\theta_s > 0$. More importantly for control, $\Delta\theta_s/\Delta L_p$ is decreasing with $\hat{L}_p$ meaning less $|\Delta\theta_s|$ when $\hat{L}_p > L_p$ than if $\hat{L}_p < L_p$. For a given $\hat{L}_p$, the $|\Delta\theta_s|$ is further reduced for the over-excited BDFRG being of most practical interest when $Q_p \leq 0$ in (13) (i.e. $|Q_p|$ production), hence $i_{pd} \leq 0$ in both (13) and (27).

The steady-state errors of the estimated position for the whole operating speed range are displayed in Fig. 5. The analytical predictions for ±25% and +10% mismatches in $\hat{L}_p$ are compared with the simulated values showing dynamic and steady-state position estimation errors, in Section 6.2.

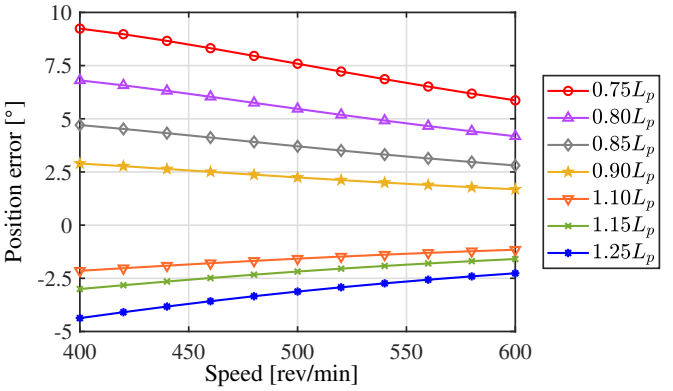

Figure 5: Analytical calculations of the control frame misalignment ($\Delta\theta_s$) using (27) for $i_{pd} = 0$ (i.e. $Q_p^{ref} = 0$ in Fig. 3).

6. Simulation and Experimental Results

The sensorless control in Fig. 3 is simulated using the BDFRG wind turbine specifications from Table 1. The Simulink® studies have been made realistic by including: discrete-time implementation, high frequency white noise and transducer dc offset in measurements, and detailed IGBT converter models. The BDFRG design particulars can be found in [11]. A real-time response of the MRAS observer in Fig. 4A, and the dedicated BDFRG controller in Fig. 3, is examined on the Hardware-In-the-Loop (HIL) test system shown in Fig. 6. The C code is compiled in dSPACE® [32, 33] from the Simulink model using the Real-Time Workshop® and ported to the DS1103 platform to be executed at 10 kHz control sampling rate i.e. switching frequency of the space-vector-pulse-width-modulated (SVM) converter. The DS1103 is built around the 32-bit PowerPC 750GX as the master processor with a 1GHz clock and the rapid control prototyping is achieved using 16-bit A/D and D/C converters and a slave Texas Instruments® TMS320F240 DSP.

Table 1
The 1.5 MW BDFRG ratings and parameters

Stator voltages (V rms)	$V_p = 690$	$V_s = 230$
Stator currents (kA rms)	$I_p = 1.1$	$I_s = 1.2$
Winding resistance (mΩ)	$R_p = 7$	$R_s = 14.2$
Winding self-inductance (mH)	$L_p = 4.7$	$L_s = 5.7$
Mutual inductance (mH)	$L_m = 4.5$	
Primary and secondary pole-pairs	$p_p = 4$	$p_s = 2$
Generator and turbine speed (rev/min)	600	20

6.1. Variable speed operation

The GE® turbine power curves for different wind and BDFRG speeds, and the drive train response to step-changes in wind speed are plotted in Fig. 7. Although such fast transients may be considered extreme even for gusty winds, they are imposed to test the controller functionality under the most challenging conditions. The $\hat{\omega}_{rm}$ to generate the MPPT reference, and both $\hat{\theta}_r$ and $\hat{\theta}_s$ for the clearly decoupled P_p and Q_p control, are provided by the observer with negligible estimation error over the range of 100 rev/min around, and down to, the synchronous speed (500 rev/min) of the BDFRG with a 6-pole rotor and 50 Hz line frequency. The Q_p is accurately controlled for the unity power factor (i.e. $Q_p^{ref} = 0$), and so is the respective i_{sd} at $i_{sd}^{ref} = v_p/(\omega_p L_m) \approx 0.4$ kA being fully responsible for the flux production with $i_{pd} = 0$ in this case given (13). The active current components, i_{sq} and i_{pq}, are essentially scaled speed dependent P_p profiles as expected from (12). They are mutually intact by the sudden variations in the i_{sd}, i_{pd} and Q_p counterparts, introduced to demonstrate the excellent disturbance rejection properties of the PI regulators. The maximum wind energy extraction has been achieved. For instance, the desired MPPT output at the rated 12 m/s

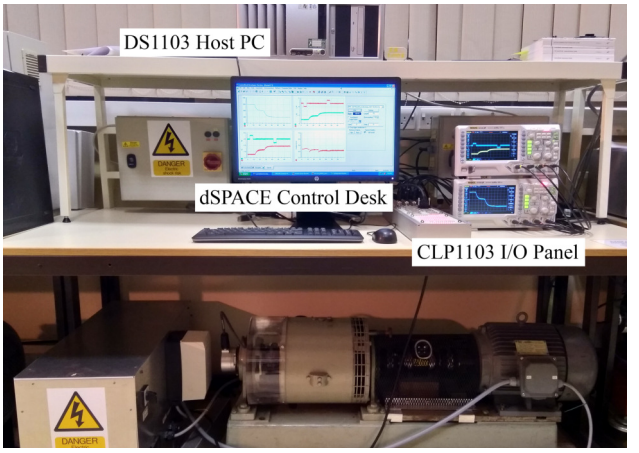

Figure 6: A HIL equipment for the BDFRG WECS emulation.

is $P_m^{ref} = -1.5$ MW as read from the corresponding turbine characteristic in the top right subplot. The secondary frequency at 600 rev/min for $a = 600/400 = 1.5$ and $f_p = 50$ Hz in (5) is $f_s = 10$ Hz. Therefore, the primary winding contribution should be $P_p^{ref} = -1.25$ MW according to (4), or the block diagram in Fig. 3, which has indeed been confirmed by the obtained P_p curves in the first 10 s. The remaining 0.25 MW is delivered to the grid by the secondary i.e. $P_s \approx 0.17 P_m$. Note the phase sequence reversal of the latter from positive to negative (i.e. $\omega_s < 0$ in Fig. 2) accompanied by the speed mode transition from super to sub-synchronous beyond 25 s time instant. For this reason, at 8 m/s and 400 rev/min, $f_s = -10$ Hz in (4) making $P_p^{ref} \approx -0.56$ MW for $P_m^{ref} \approx -0.45$ MW. The secondary side again provides the necessary power balance, but consuming 0.11 MW this time i.e. $P_s \approx 0.24|P_m|$. Finally, there is a very close correlation between the real-time (captured on oscilloscopes as shown in Fig. 6) and simulated back-to-back waveforms in Fig. 7. Similar comments on the observer high accuracy, decoupled control, bi-directional secondary power flow, and winding participation in the energy conversion, can be made from Fig. 8.

6.2. Parameter sensitivity studies

The latest review of the parameter identification procedures for the most promising 8/4-pole BDFRG type has reported < 10% relative differences between the experimental and design predictions for L_m, and < 5% for L_p [34]. Nevertheless, a variance of up to 30% in $\hat{L}_m$, and 25% in $\hat{L}_p$, has been assumed to demonstrate the observer and controller robustness. For ease of comparisons, the same wind speed and ± 0.3 MVAr step reference signals have been simulated as in Fig. 7 produced using the actual L_m and L_p values from Table 1.

The observer salient features discussed in Sections 4 and 5 have been validated by the results presented in Fig. 9. The complementary remarks are as follows: (1) The rotor speed estimation errors ($\Delta\omega_{rm}$) are zero in average by analogy to Fig. 7 despite the severe inductance mismatches ($|\Delta L_{m,p}|$). The secondary current vector angular displacement (Fig. 4B) is minor too (e.g. mean $|\delta_{err}| \approx 0.25°$), the plots being nearly identical in all cases so only one is shown in Fig. 9e. Such precise $\hat{\omega}_{rm} = \hat{\omega}_r / p_r$ and $\hat{\delta}$ are imperative for the algorithm convergence and can be largely attributed to the adaptive PI control actions coupled with the closed-loop observer design (Fig. 4A), meaning that the main stability criteria (i.e. $\Delta\omega_r \approx 0$ and $\varepsilon \approx 0$), coming from (20)-(22) have been satisfied; (2) The position estimates ($\hat{\theta}_{r,s}$), although inferior to those in Fig. 7 as expected, are of sufficiently high quality, the respective errors ($\Delta\theta_r = \Delta\theta_s$) gradually increasing in absolute sense with lowering $\hat{L}_p$ for a given $|\Delta L_p|$. This can be seen in Figs. 9a and 9h for $|\Delta L_p| = 0.25 L_p$, as well as from Fig. 5 in steady-state; (3) $\Delta\theta_s$ is unaffected by $\hat{L}_m$ inaccuracies, and so is the $\hat{\theta}_s$ dependent current control performance (Fig. 3), as per Figs. 9f-h showing the entirely coincident waveforms for either $\hat{L}_m$; (4) The $\hat{L}_{m,p}$ variations have a notable impact on the $\hat{i}_s$ accuracy, which is much worse than in Fig. 7, as illustrated in Fig. 9l. However, this drawback is irrelevant to control as the secondary current measurements are used to derive the feedback components ($i_{sd,q}$) as indicated in Fig. 3; (5) The decoupled P_p and Q_p characteristics in Fig. 9d, generated from the measured primary voltages and currents (Fig. 3), are basically the same as in Fig. 7 and do not seem to be influenced by $\Delta\theta_s$ even for the maximum $|\Delta L_{m,p}|$ considered; (6) The corresponding $i_{sq} = i_s \sin\hat{\gamma}$ and $i_{sd} = i_s \cos\hat{\gamma}$ in Fig. 9b are also little affected by the relatively small $|\Delta\theta_s|$ (i.e. below 10% from Fig. 9c), and even less according to

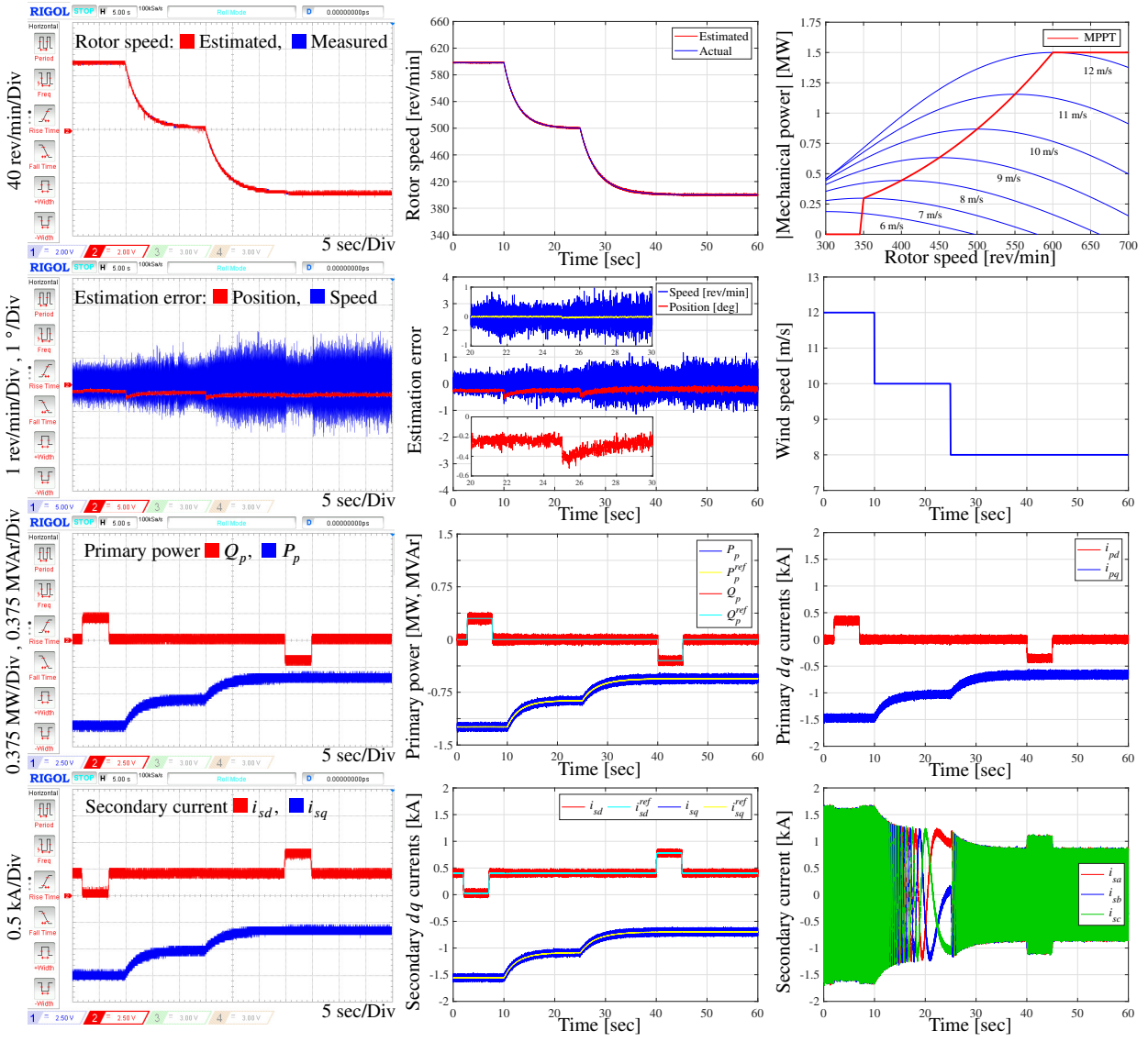

Figure 7: Oscillograms and simulated waveforms of the BDFRG sensorless control performance.

Figs. 9f and 9k, closely resembling the counterparts in Fig. 7; (7) The effects of the $\Delta\theta_s$ introduced secondary frame misalignment on the current control quality are quantified in Figs. 9c, 9f and 9k through $\Delta i_{sd} = i_s \cos\gamma - i_{sd}$ and $\Delta i_{sq} = i_s \sin\gamma - i_{sq}$ where $\hat{\gamma} = \gamma + \Delta\theta_s$ as outlined in Fig. 4B. It is clearly visible that both $|\Delta i_{sd}|$ and $|\Delta i_{sq}|$, normalised to the measured i_s, are very similar in shape to $|\Delta\theta_s|$ shown in the top three sub-plots, all rising in magnitude with the speed reduction (pertaining to the profile in Fig. 7) and varying in a wider range for the under-estimated $\hat{L}_p$ (e.g. the changes are bigger in Fig. 9a than in Fig. 9h, and the least in Fig. 9i at only 10% mismatch). This is also evident from Fig. 5, which can provide reasonable $\Delta\theta_s$ approximations for a given $\hat{L}_p$ at unity (as presented) or any other primary power factor of interest determined by i_{pd} in (27); (8) Finally, note in Fig. 9 the favorable dips in the $|\Delta\theta_s|$ responses to the $Q_p < 0$ step changes i.e. when $|Q_p|$ is being delivered to the grid as desired in practice.

6.3. Two-mass mechanical model

The simulated wind turbine represents a simplified model of the actual electro-mechanical WECS. The effect of more detailed mechanical modelling on the MRAS performance is evaluated using a two-mass model shown in

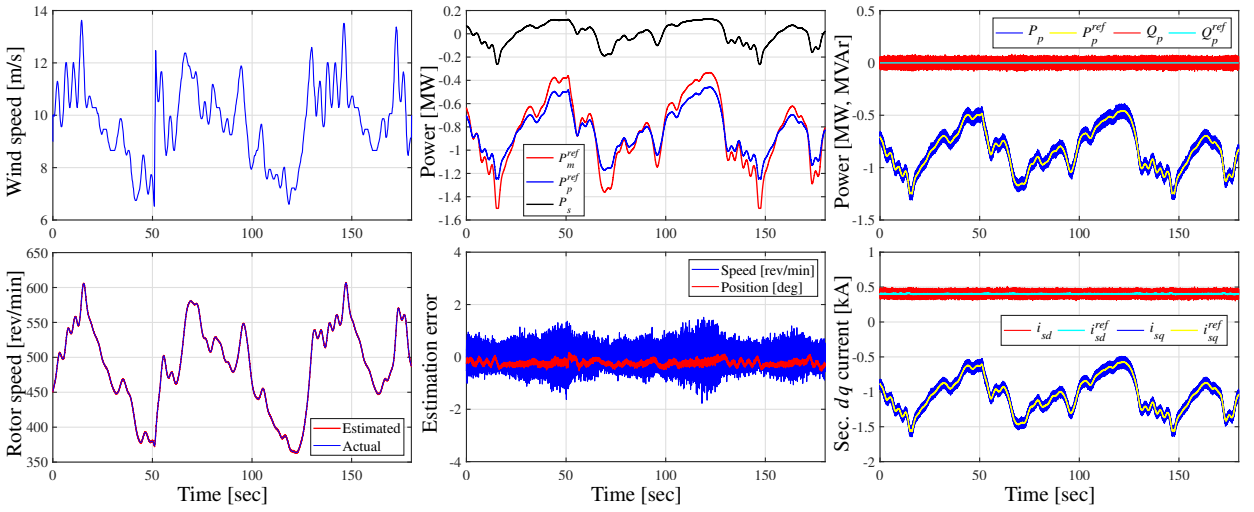

Figure 8: Sensorless MPPT operation of the BDFRG turbine for a realistic wind speed profile.

Fig. 10-A [35, 36]. The corresponding model of the drive train dynamics presented in Fig. 10-B uses separate masses for the turbine (H_{wt}) and generator (H_g). The effective shaft torsional stiffness (K_{sh}) and mutual damping (D_m) model the dynamics of the coupling between the low-speed turbine and the medium-speed BDFRG. The comparative simulation studies of the two-mass and single-mass models of the drive train are presented in Fig. 11 when the wind speed is changed suddenly from 9 m/s to 11 m/s at $t = 5$ s. This observation proves that the accuracy of the speed and angle estimation of the MRAS observer is unaffected by the mechanical dynamics. As shown in Fig. 1, the grid-side-converter (GSC) regulates the DC link voltage and injects additional reactive power to the grid, which is very similar to the DFIG counterpart [19, 37]. Thus, the MRAS observer performance is not impacted by the GSC modelling and is out of scope of this paper.

6.4. Symmetrical fault studies

The transient performance of the proposed MRAS observer is evaluated during a 20% symmetrical voltage dip lasting 2.5 s [38] at a constant wind speed of 11 m/s. The two-mass model is applied to take the mechanical dynamics into account for the speed and position estimation. As shown in Fig. 12, the observer is able to provide accurate position estimates (within a 5° margin) with zero steady-state speed error during the fault and after recovery. The transient speed estimation errors at the fault inception and clearance time instants are less than 2.2%, which proves the accuracy and effectiveness of the proposed observer.

7. Conclusions

A new, viable MRAS based estimation technique for sensorless control of real (P_p) and reactive power (Q_p) of large-scale BDFRG wind turbines has been presented and verified by realistic simulation, experimental, and sensitivity studies to parameter uncertainties. The results produced for a custom 1.5 MW BDFRG design of comparatively negligible resistances have shown the outstanding performance prospects in terms of the entirely decoupled P_p and Q_p responses and intrinsic robustness of the controller to disturbances created by step-changes in Q_p demands, variable MPPT conditions, and/or significant inductance variations. Such attractive attributes have been made possible by the accurate estimates of the control frame position, and foremost the rotor speed, offered by the observer strong advantages over the existing configurations including a highly reliable reference model, reliant on the secondary current measurements only, and a closed-loop adaptive counterpart requiring knowledge of the measured grid voltages and currents at line frequency, and the primary winding self ($\hat{L}_p$) and mutual ($\hat{L}_m$) inductances identified by off-line testing or otherwise. The properly tuned PI gains, arriving from a small-signal analysis, have allowed to: (1) eliminate inaccuracies in the adaptive model outputs; (2) preserve the stability of the observer, hence the control algorithm; (3) accomplish the $\hat{L}_m$ independence in the process; and (4) achieve immunity to $\hat{L}_p$ mismatches, especially in the

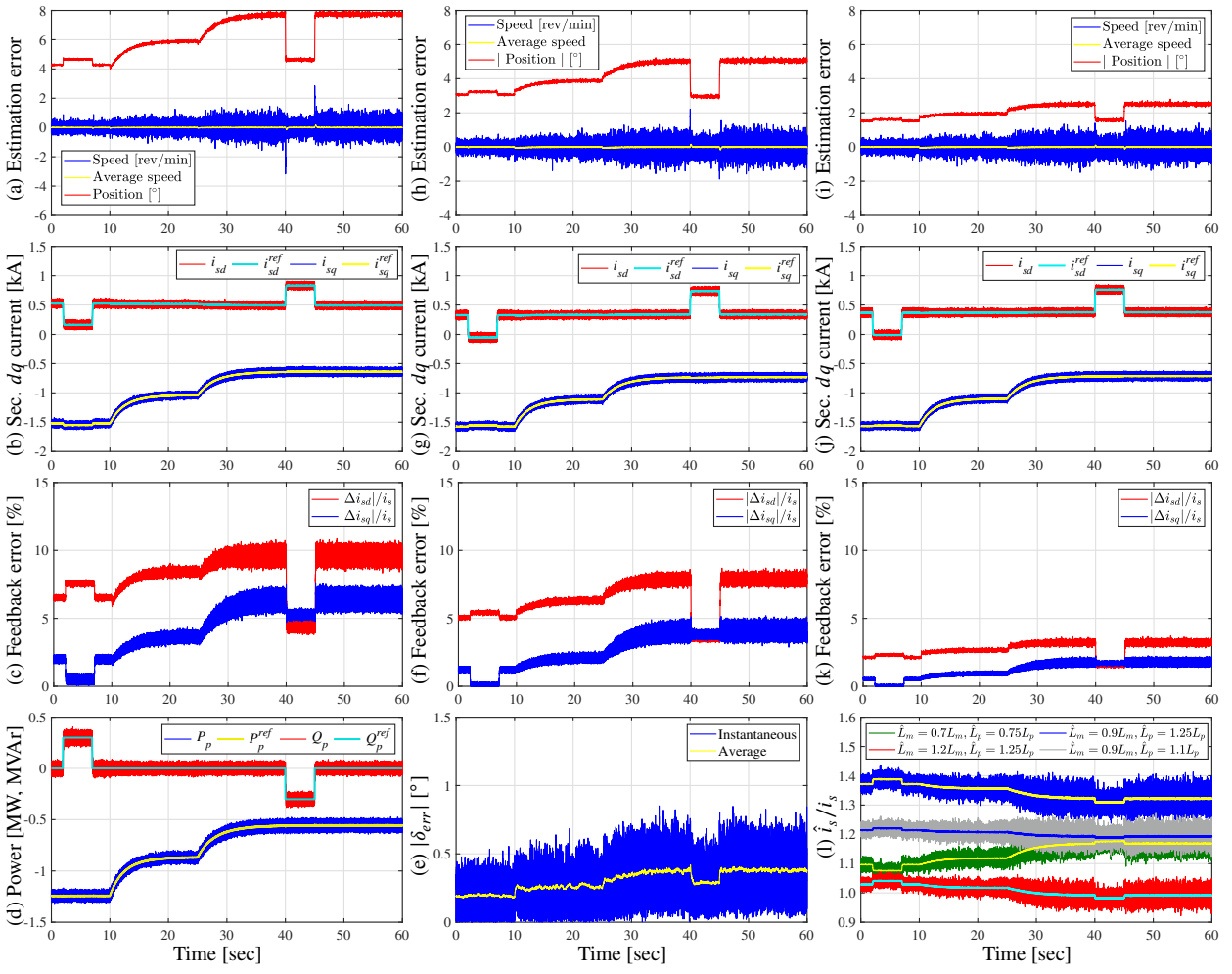

Figure 9: The observer and BDFRG controller responses to inductance mismatches: (a-e) $\hat{L}_m = 0.70L_m$, $\hat{L}_p = 0.75L_p$; (f-h) $\hat{L}_m = 1.20L_m$ & $\hat{L}_m = 0.90L_m$, $\hat{L}_p = 1.25L_p$; (i-k) $\hat{L}_m = 0.90L_m$, $\hat{L}_p = 1.10L_p$; (l) current ratio comparison.

most efficient super-synchronous mode of the Q_p producing BDFRG, when the overall little position estimation (and associated current feedback) errors turn out to be the smallest.

The above observer and controller properties are indeed stimulating to justify continuing BDFRG research as a promising medium-speed DFIG substitute. The operation and maintenance cost savings that can be made by its brushless construction, the absence of a vulnerable shaft position sensor, and the use of a simpler 2-stage gearbox, should undoubtedly be appealing arguments to consider for grid-connected wind power applications down the line.

References

[1] M. Asghar, Nasimullah, Performance comparison of wind turbine based doubly fed induction generator system using fault tolerant fractional and integer order controllers, Renew. Energy 116 (2018) 244 – 264.

[2] N. E. Karakasis, C. A. Mademlis, High efficiency control strategy in a wind energy conversion system with doubly fed induction generator, Renew. Energy 125 (2018) 974 – 984.

[3] S. Li, Reliability models for DFIGs considering topology change under different control strategies and components data change under adverse operation environments, Renew. Energy 57 (2013) 144 – 150.

[4] M. F. Hsieh, Y. H. Chang, D. Dorrell, Design and analysis of brushless doubly-fed reluctance machine for renewable energy applications, IEEE Trans. Magnetics 52 (7) (July 2016).

[5] F. Zhang, H. Wang, G. Jia, D. Ma, M. G. Jovanovic, Effects of design parameters on performance of brushless electrically excited synchronous reluctance generator, IEEE Trans. Indust. Electron. 65 (11) (2018) 9179–9189.

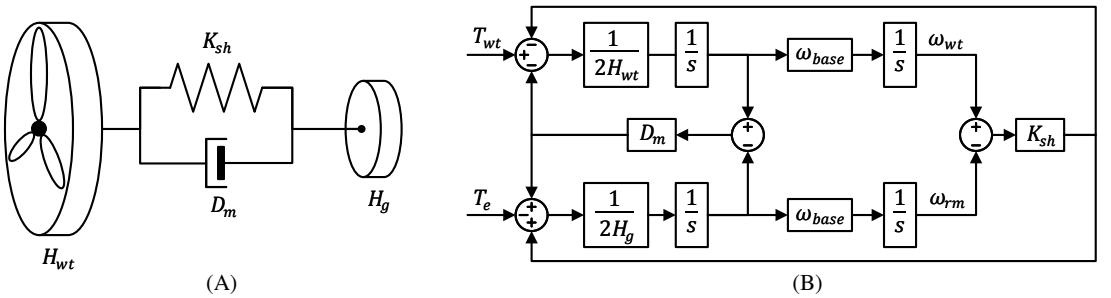

Figure 10: Two-mass mechanical model of BDFRG-based wind turbine: A) Schematics; B) Block diagram.

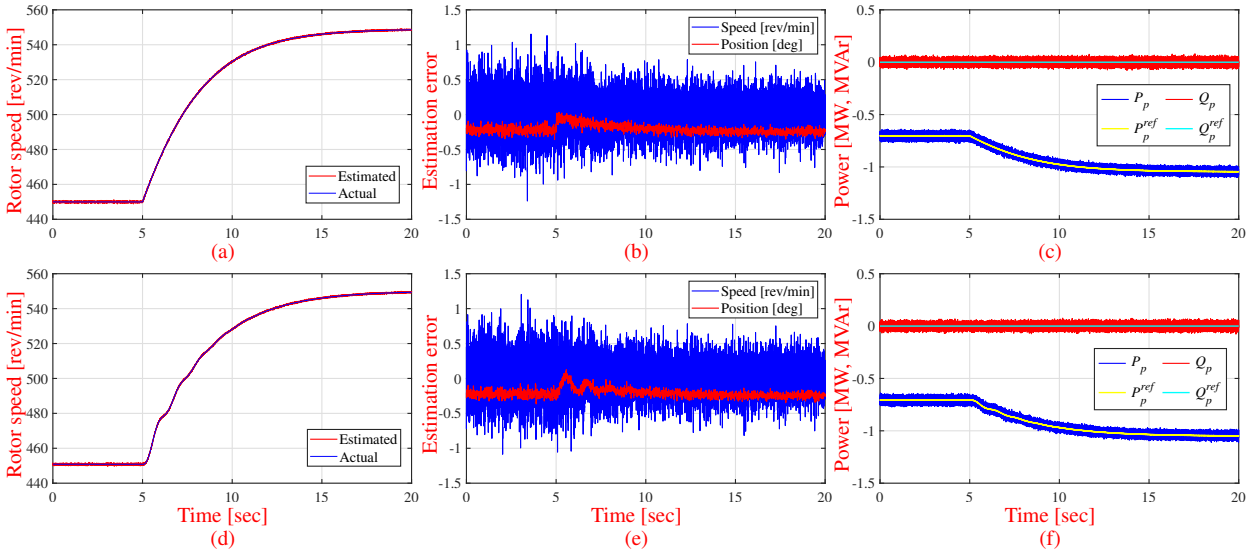

Figure 11: Comparative simulation results of the two-mass and single-mass turbine models.

[6] L. Zhu, F. Zhang, S. Jin, S. Ademi, X. Su, W. Cao, Optimized power error comparison strategy for direct power control of the open-winding brushless doubly fed wind power generator, IEEE Trans. Sustain. Energy 10 (4) (2019) 2005–2014.

[7] P. Han, M. Cheng, S. Ademi, M. G. Jovanovic, Brushless doubly-fed machines: Opportunities and challenges, Chinese Journal of Elect. Engineering 4 (2) (2018) 1–17.

[8] Y. Li, S. Valla, E. Zio, Reliability assessment of generic geared wind turbines by GTST-MLD model and monte carlo simulation, Renew. Energy 83 (2015) 222 – 233.

[9] F. Zhang, S. Yu, Y. Wang, S. Jin, M. G. Jovanovic, Design and performance comparisons of brushless doubly-fed generators with different rotor structures, IEEE Trans. Indust. Electron. 66 (1) (2019) 631–640.

[10] M. Cheng, P. Han, G. Buja, M. G. Jovanović, Emerging multiport electrical machines and systems: Past developments, current challenges, and future prospects, IEEE Trans. Indust. Electron. 65 (7) (2018) 5422–5435.

[11] A. Attya, S. Ademi, M. Jovanovic, O. Anaya-Lara, Frequency support using doubly fed induction and reluctance wind turbine generators, Inter. Journal of Elect. Power and Energy Syst. 101 (2018) 403–414.

[12] H. Chaal, M. Jovanovic, Power control of brushless doubly-fed reluctance drive and generator systems, Renew. Energy 37 (1) (2012) 419–425.

[13] S. Raju, G. Pillai, Design and real time implementation of type-2 fuzzy vector control for DFIG based wind generators, Renew. Energy 88 (2016) 40 – 50.

[14] S. Ademi, M. Jovanović, Vector control methods for brushless doubly fed reluctance machines, IEEE Trans. Indus. Electron. 62 (1) (2015) 96–104.

[15] S. Ademi, M. Jovanović, M. Hasan, Control of brushless doubly-fed reluctance generators for wind energy conversion systems, IEEE Trans. Energy Convers. 30 (2) (2015) 596–604.

[16] S. Ademi, M. Jovanovic, Control of doubly-fed reluctance generators for wind power applications, Renew. Energy 85 (2016) 171–180.

[17] M. Morawiec, K. Blecharz, A. Lewicki, Sensorless rotor position estimation of doubly fed induction generator based on backstepping technique, IEEE Trans. Indust. Electron. 67 (7) (2020) 5889–5899.

[18] O. Barambones, J. A. Cortajarena, I. Calvo, J. M. Gonzalez de Durana, P. Alkorta, A. Karami-Mollaee, Variable speed wind turbine control

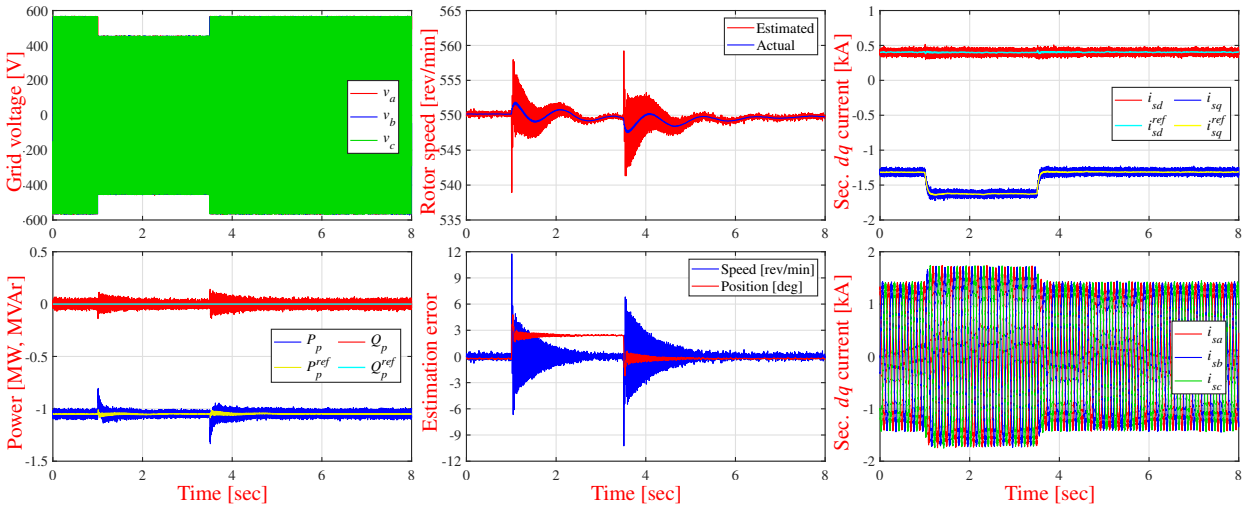

Figure 12: Controller and MRAS performance during a 20% symmetrical voltage dip.

scheme using a robust wind torque estimation, Renew. Energy 133 (2019) 354 – 366.

[19] R. Nair, G. Narayanan, Stator flux based model reference adaptive observers for sensorless vector control and direct voltage control of doubly-fed induction generator, IEEE Trans. Indus. Appl. 56 (4) (2020) 3776–3789.

[20] A. T. Nguyen, D. C. Lee, Sensorless control of DFIG wind turbine systems based on SOGI and rotor position correction, IEEE Trans. Power Electron. 36 (5) (2020) 5486 – 5495.

[21] A. Giannakis, A. Karlis, Y. L. Karnavas, A combined control strategy of a DFIG based on a sensorless power control through modified phase-locked loop and fuzzy logic controllers, Renew. Energy 121 (2018) 489 – 501.

[22] L. Lu, N. F. Avila, C. Chu, T. Yeh, Model reference adaptive back-electromotive-force estimators for sensorless control of grid-connected DFIGs, IEEE Trans. Indust. Appl. 54 (2) (2018) 1701–1711.

[23] B. Bossoufi, M. Karim, A. Lagrioui, M. Taoussi, A. Derouich, Observer backstepping control of DFIG-generators for wind turbines variable-speed: FPGA-based implementation, Renew. Energy 81 (2015) 903 – 917.

[24] M. Jovanovic, S. Ademi, R. Binns, Sensorless variable speed operation of doubly-fed reluctance wind generators, IET Renew. Power Gener. (2020) 1–10.

[25] S. Ademi, M. G. Jovanović, H. Chaal, W. Cao, A new sensorless speed control scheme for doubly fed reluctance generators, IEEE Trans. Energy Conver. 31 (3) (2016) 993–1001.

[26] K. Kiran, S. Das, M. Kumar, A. Sahu, Sensorless speed control of brushless doubly-fed reluctance motor drive using secondary flux based MRAS, Electric Power Components and Syst. 46 (6) (2018) 701–715.

[27] M. Kumar, S. Das, K. Kiran, Sensorless speed estimation of brushless doubly-fed reluctance generator using active power based MRAS, IEEE Trans. Power Electron. 34 (8) (2019) 7878–7886.

[28] M. R. Agha Kashkooli and M. G. Jovanović, Sensorless MRAS Control of Brushless Doubly-Fed Reluctance Generators for Wind Turbines 2020 International Conference on Electrical Machines (ICEM) 1 (2020) 202–2208.

[29] J. Carroll, A. McDonald, D. McMillan, Reliability comparison of wind turbines with DFIG and PMG drive trains, IEEE Trans. Energy Conver. 30 (2) (2015) 663–670.

[30] I. Boldea, L. Tutelea, Reluctance Electric Machines: Design and Control, CRC Press, Boca Raton, U.S., 2018.

[31] R. E. Betz, M. G. Jovanović, Introduction to the space vector modelling of the brushless doubly-fed reluctance machine, Electric Power Components and Syst. 31 (8) (2003) 729–755.

[32] DS1103 PPC Controller Board: Hardware Installation and Configuration, dSPACE GmbH, Paderborn, Germany, 2014.
URL www.manualslib.com/manual/1666045/Dspace-Ds1103.html

[33] S. Mensou, A. Essadki, T. Nasser, B. B. Idrissi, L. Ben Tarla, Dspace DS1104 implementation of a robust nonlinear controller applied for DFIG driven by wind turbine, Renew. Energy 147 (2020) 1759 – 1771.

[34] D. Gay, R. E. Betz, D. Dorrell, A. Knight, Brushless doubly fed reluctance machine testing for parameter determination, IEEE Trans. Indust. Appl. 55 (3) (2019) 2611–2619.

[35] N. W. Miller, J. J. Sanchez-Gasca, W. W. Price, R. W. Delmerico, Dynamic modeling of GE 1.5 and 3.6 MW wind turbine-generators for stability simulations 3 (2003) 1977–1983..

[36] I. P. Girsang, J. S. Dhupia, E. Muljadi, M. Singh, L. Y. Pao, Gearbox and drivetrain models to study dynamic effects of modern wind turbines, IEEE Trans. Indust. Appl. 50 (6) (2014) 3777–3786.

[37] S. Yang, V. Ajjarapu, A speed-adaptive reduced-order observer for sensorless vector control of doubly fed induction generator-based variable-speed wind turbines, IEEE Trans. Energy Conver. 25 (3) (2010) 891–900.

[38] The grid code, National Grid Electricity Transmission plc., London, United Kingdom, 2017.

1 URL www.nationalgrid.com/sites/default/files/documents/8589935310-CompleteGridCode.pdf